Probing lithium-ion batteries' state-of-charge using ultrasonic transmission — Concept and laboratory testing

Lukas Gold [a, *], Tobias Bach [a, 1], Wolfgang Virsik [a], Angelika Schmitt [a], Jana Müller [a], Torsten E.M. Staab [a, b], Gerhard Sextl [a, b]
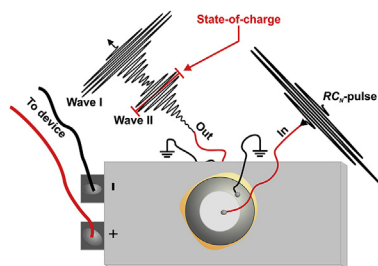
[a] Fraunhofer Institute for Silicate Research ISC, Neunerplatz 2, 97082, Würzburg, Germany
[b] University of Würzburg, Chair of Chemical Technology of Materials Synthesis, Röntgenring 11, 97070, Würzburg, Germany

HIGHLIGHTS

- Physical method to detect the state-of-charge of lithium-ion batteries.
- Theoretical framework built on poromechanics.
- Mechanical properties as an additional source for information on the state-of-charge.
- Low cost alternative for charge bookkeeping and voltage tracking.

GRAPHICAL ABSTRACT

ARTICLE INFO

ABSTRACT

For electrically powered applications such as consumer electronics and especially for electric vehicles a precise state-of-charge estimation for their lithium-ion batteries is desired to reduce aging, e.g. avoiding detrimental states-of-charge. Today, this estimation is performed by battery management systems that solely rely on charge bookkeeping and cell voltage measurements. In the present work we introduce a new, physical probe for the state-of-charge based on ultrasonic transmission. Within the simple experimental setup raised cosine pulses are applied to lithium-ion battery pouch cells, whose signals are sensitive to changes in porosity of the graphite anode during charging/dis-charging and, therefore, to the state-of-charge. The underlying physical principle can be related to Biot's theory about propagation of waves in fluid saturated porous media and by including scattering by boundary layers inside the cell.

© 2017 Elsevier B.V. All rights reserved.

1. Introduction

1.1. Motivation

The transition from short-lived, disposable batteries to advanced portable and stationary high power-density battery systems, e.g. for electric transportation or storage applications, has raised reasonable interest in their lifetime, i.e. the aging of battery cells. For the most common lithium-ion battery types it was found that, varying the lithiation of graphite, i.e. the state-of-charge (SoC), during cycling, has the biggest impact on battery aging and, therefore, is responsible for lifetime limitation [1–3]. Thus, the state-of-charge estimation is one of the most important features of today's battery management systems (BMS) [4,5]. Its implementation is quite complex [6,7] involving mathematical algorithms like Kalman filters to extract the desired information from charge bookkeeping and measuring the voltage response to power

consumption. As this requires expensive BMS hardware, an alternative and possibly lower cost system is highly desired.

Detailed research on the origin of battery aging [8–11] has proven that the intercalation of lithium into graphite, going along with volume changes, is an essential cause for degradation. Thus, by correlating mechanical properties of lithium-ion batteries to the degree of graphite lithiation one can determine the SoC. However, most of the published studies rely on measurements of battery thickness [12,13] and stress [14,15], whereas only one alternative route employing acoustic measurements in transmission and reflection geometry at 2.25 MHz was published by Hsieh et al. [16]. In contrast to their study, the present work relies solely on measurements of transmitted ultrasonic pulses and utilizes a different range of frequencies. In this study we will show that the ultrasonic pulse transit time from transmitter to receiver piezo, the so called time-of-flight (ToF), and its amplitude are depending linearly on the SoC. This makes ultrasonic measurements feasible for the SoC estimation.

1.2. Theory of ultrasonic probing

To analyze materials by ultrasound waves, *raised* cosine *pulses* with N oscillations (RC_N-pulses) are commonly used [17]. An RC_N-pulse has an envelope function with a length of $2\pi N/\omega_0$, where ω_0 is the circular frequency:

$$RC_N(t) = \begin{cases} \left[1 + cos\left(\dfrac{\omega_0 t}{N}\right)\right] cos(\omega_0 t)\ for\ |t| \leq \dfrac{N\pi}{\omega_0} \\ \qquad\qquad 0\ for\ |t| \geq \dfrac{N\pi}{\omega_0}. \end{cases} \tag{1}$$

The travel of sound through heterogeneous materials is usually classified by different modes: mainly pressure and shear waves. These modes differ with the media traversed, e.g. fluid and/or particles, causing different displacement either being longitudinal (pressure waves, also called dilatational or compressional waves), or transversal (shear waves, also called rotational waves) [18,19]. A theoretical description of the transmission of ultrasound through lithium-ion batteries assumes these porous structures to be completely filled with electrolyte. Therefore, we describe acoustic waves in fluid-saturated porous media considering the relative motion of the porous frame and the fluid. Based on the above described assumption, the theoretical framework is given by Biot's "Theory of Propagation of Elastic Waves in a Fluid-Saturated Porous Solid" [18,19]. Biot was able to show within certain assumptions that indeed three waves, one shear wave and two pressure waves exist in the absence of dissipative forces [20]. Here, we will concentrate on the pressure waves, which are labeled *fast wave* and *slow wave*. The former exhibits in-phase displacement in solid and fluids, whereas for the latter displacement of solid and liquid are of opposite phase.

To estimate attenuation, Biot describes dissipation assuming *Poiseuille flow* in the fluid with the laminar regime, which is valid for sufficiently small $Re = (inertial\ forces)/(viscous\ forces)$ (dimensionless Reynolds number). Based on a consideration of the quarter wavelength of the boundary layer above an oscillating planar surface the critical frequency, also called transition frequency, $f_t = (\pi\ \nu)/(4\ d^2)$ for breakdown of *Poiseuille flow* is derived by Biot, where ν denotes the kinematic viscosity and d the pore diameter [18,19]. Assuming a typical kinematic viscosity $\nu = 24\ \mu m^2\ s^{-1}$, e.g. EC/DMC/LiPF$_6$ representing a standard electrolyte at room temperature, a typical particle size of maximum 10 μm and an electrode thicknesses in the order of 0.1 mm, one can roughly estimate the

critical frequency f_t to be as high as 1.6 MHz. This is based on the assumption of spherical, closed packed graphite particles, whose biggest pores have diameters of approximately 4 μm [21]. It follows that any ultrasonic frequency utilized in this work can be considered "low", if it is at least one order of magnitude lower than the critical frequency f_t. As shear and pressure waves can be considered to be uncoupled, Biot has given formulas valid for frequencies approximately one order of magnitude below the critical frequency, i.e. denoted as "low". However, those rely on additional assumptions which are under debate for their appropriateness (see Jocker et al. [22]).

Based on these approximations for the velocities of shear and pressure waves V_s and V_I, V_{II}, respectively, one can predict acoustic properties for a wide range of materials. Biot showed that for frequencies, considered "low", relative deviations of V_I from the reference velocity V_c are in the order of 10^{-4}. Therefore, they can be assumed to be identical [19], which is applied in this work if not otherwise stated: $V_I \cong V_c = \sqrt{H/\rho}$, with Biot's coefficient H and the mean density ρ.

The velocities V_{II} and V_s are calculated based on the parameters listed in Appendix A, where σ denotes parameters defining elastic properties, γ parameters of dynamic properties, f the frequency, f_c the characteristic frequency and N_n the shear modulus of the drained porous matrix [19]:

$$V_{II} = V_c \sqrt{2\frac{f}{f_c}\frac{\sigma_{11}\ \sigma_{22} - \sigma_{12}^2}{\gamma_{12} + \gamma_{22}}}. \tag{2}$$

Biot's predictions of acoustic velocities in fluid-filled porous media have been validated in several applications [23–29]. Thus, when additionally including some adaptions for stratified (layered) porous media [30–32], they are suitable for battery applications. Estimations of attenuation derived from this theory are generally less successful. This can be explained by difficulties in defining the correct parameters [33] and competing attenuation mechanisms such as squirt-flow [33–37], wave induced flow on larger scales [38,39] or viscous shear relaxation [33,40]. Especially in stratified media, the transmitted signal can be highly dependent on the ratio between wavelength and the periodic length of the material [41].

Theoretical studies predict heavy variations depending on the type of stratifications, leading to transitional regimes with abruptly increasing or decreasing attenuation [41–43] as well as attenuation peaks [37,44]. In layered systems periodic effects have been observed as well [22]. Jocker et al. investigated the transmission of acoustic pulses through stratified, fluid-filled porous materials and concluded that "[s]ince the slow compressional wave has the shortest wavelength, scattering effects will first affect this wave type before affecting others" [22]. According to these predictions the ultrasonic transmission signal may contain variant and invariant parts depending on physical and mechanical properties of the stratified porous media – here: lithium-ion batteries – as will be shown in the following.

2. Experimental

2.1. Test samples

To validate the determination of the SoC based on ultrasonic detection of graphite's volume expansion, commercial cells with state-of-the-art energy and power density were chosen. This method has been tested by our group on pouch cells of various types, e.g. lithium graphite||lithium-cobalt-oxide based LIBs, and

graphite||lithium-iron-phosphate based LIBs as they exhibit a very flat voltage profile which makes an alternative SoC estimation even more interesting. This work concentrates entirely on high power pouch-type cells with a capacity of 1.2 Ah from Conrad-energy. All cells called pristine in this article have undergone a formation procedure at the discretion of the manufacturer. Key specifications are listed in Appendix B, Table B 1. The batteries were charged and discharged in steps of 20% of nominal capacity using a current of 2 C and 4 C, respectively, in order to prepare well defined SoCs. Cyling of batteries as well as laboratory measurements were performed at room temperature (25 °C). For reproduction of results, at least three cells, as received from manufacturer, were used during experiments. Figures show exemplary results for one battery.

2.2. Laboratory measurements

In order to probe changes in ultrasonic transmission due to intercalation and deintercalation of lithium in graphite, short ultrasonic pulses were used. Raised cosine filtered pulses (RC_N-pulses) were used because of their favorable frequency and time domain properties. Separate transducers were used for signal generation and detection of the answer. Their placement on the cell is shown in Fig. 1. The piezo elements *"Piezokeramisches Element EPZ-Serie - 6400 Hz"*, were obtained from Conrad Electronic SE. Transducers were glued centrally on the large surfaces of the prismatic cells using a commercial epoxy resin based adhesive. The resin was hardened for 24 h at room temperature. Key specifications of the transducers and the adhesive can be found in Appendix B, Table B 2 and Table B 3.

Using a custom ultrasonic sending and receiving unit "MAS-Messsystem" with variable gain and digital control of the waveform through the proprietary software CANWARE08_ISC, both obtained from Fraunhofer IKTS, an RC_N pulse with the number of oscillations $N = 5$ was then sent by the transducer acting as a speaker and transmitted through the battery. The transmitted response was received after hardware triggering by the transducer placed opposite to the piezo buzzer creating the signal pulse. The sent signal was sampled with 18.75 MSa s^{-1} and amplified with 18 dB. The received answer signal was recorded from 9.6 μs before the trigger and 1 ms after the trigger and was amplified with a gain of 18 dB and a sample rate of 4.17 MSa s^{-1}.
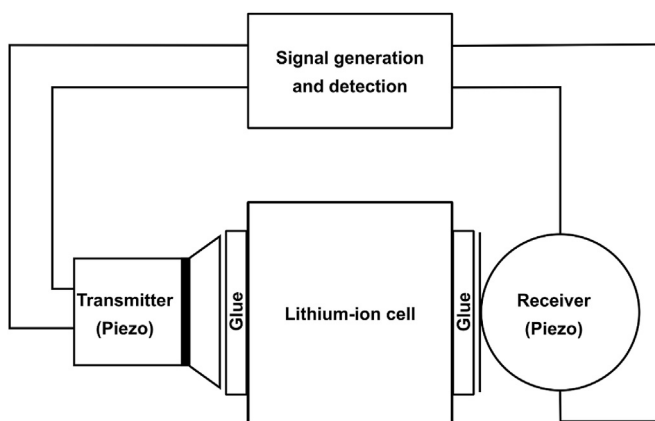

Fig. 1. Schematic drawing of the setup used for ultrasonic probing. Transmitter and receiver are placed in the center of the large faces of the cell to avoid edge effects. The piezo elements used as transducers are glued to the surface for improved reversibility.

3. Results and discussion

3.1. Measure for the state-of-charge

3.1.1. Data processing of typical signals

A pouch-type lithium-ion cell with a capacity of 1.2 Ah was equipped with two piezo transducers by gluing them onto opposite surfaces as shown in Fig. 1 and described in detail in Section 2. Pulses with a frequency of 200 kHz were passed through the cell in fully discharged and fully charged state. The response to these pulses is plotted as signal height over delay time after sending the pulse. As shown in Fig. 2 a), two major wave packets were obtained for the fully charged state.

Independent of the charge state, the first wave's amplitude is not affected. In contrast, the second wave shows a dependence on state-of-charge. The maximum amplitude is reduced to (14.08±0.61) % compared to the charged state. In the discharged state the maximum is found at (101.47±0.66) μs while in the charged state the maximum is at (88.53±0.99) μs. The waves are well separated in time making it easy to distinguish them. Within the tested frequencies, ranging from 100 kHz to 250 kHz, the behavior at 200 kHz appears to be most favorable and has been examined in more detail.

3.1.2. Characteristics of the amplitude of the answer signal

The prominent change in amplitude and the difference in transit time at 200 kHz allow for easy discrimination between charged and discharged states. In order to simplify the data, they are converted to an unsigned format. Moderate smoothing, obtained with 24 μs wide Savitzky-Golay filter of second polynomial order further simplifies the signals and increases robustness against high frequency noise. While these operations could in principle be carried out using analogue circuitry, in this work, they were carried out by digital post processing. A smoothed representation of the signals modulus is shown in Fig. 2 b). For the charged state three peaks are visible. For the cell in discharged state the first peak is nearly unchanged in the answer signal. Also the small shoulder with 50 μs delay time appears to be virtually unchanged. However, in contrast the third peak associated to the slow wave with an approximate delay of 90 μs has nearly vanished completely.

To estimate the state-of-charge, other properties of the signal besides the maximum value of the third peak may be used. The apparent delay of the peak also shows a dependence on the state-of-charge. Different analytical methods to extract the SoC information may be preferable depending on the application and hardware situation.

In order to prepare the battery for SoC estimation, the battery was charged, as described in detail in section 2.1, in steps of 20%. After each charging step, the cell was probed using an ultrasonic pulse with the answer signals being rectified and moderately smoothed. This smoothing was again obtained with 24 μs wide Savitzky-Golay filter of second polynomial order. Fig. 3 a) shows the processed signals collected during charging. The response can be divided into two parts: the early response with delays up to 70 μs and the later response containing SoC-relevant signals up to 120 μs after sending the pulse. As illustrated by the dashed blue line, the first part of the signal is invariant with respect to the state-of-charge of the cell. On the other hand, the solid red line drawn over the maximum peak height of the second part of the signal shows without doubt a dependence on the state-of-charge, i.e. a clearly positive correlation.

3.1.3. Time-of-flight method

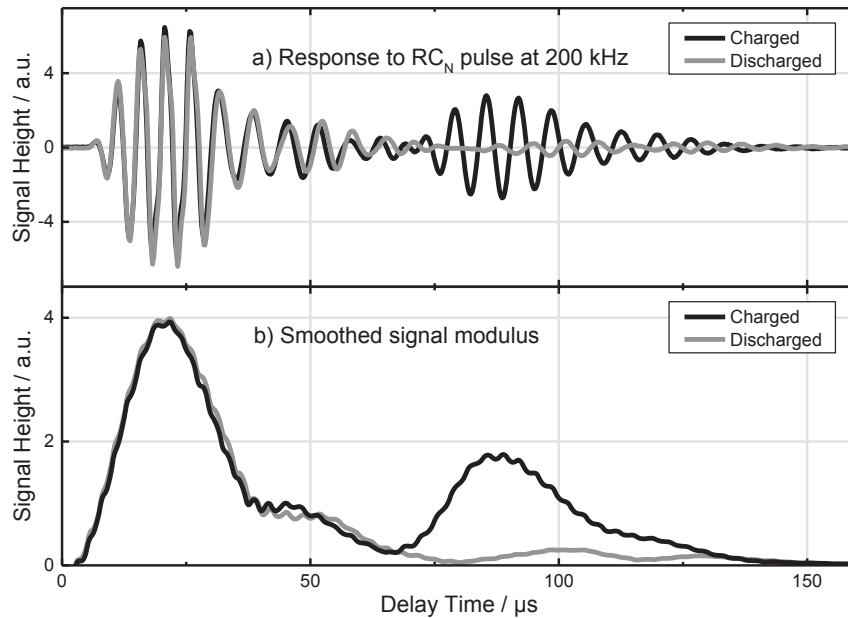Interestingly, the relative delay of the peaks can be used in a

Fig. 2. Transmission of RC_N-pulses through a lithium-ion battery pouch cell in fully charged and fully discharged state: Experimental parameters are described in Section 2. The signal height is plotted over the delay time after sending a pulse. a) Response to RC_N pulse with a frequency of 200 kHz. The obtained waveforms contain invariant and responsive parts. b) Smoothed modulus of the transmitted signal highlighting the invariant and state-dependent parts of the signals. Smoothing was obtained with 24 μs wide Savitzky-Golay filter of second polynomial order.
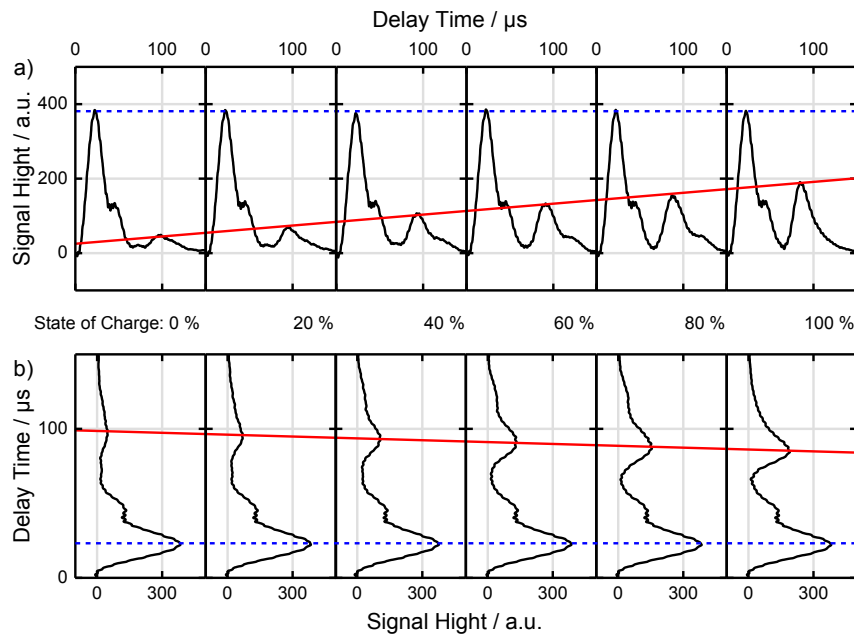

Fig. 3. Smoothed modulus of the transmitted signal of RC_N-pulses through a lithium-ion battery pouch cell: the SoC was changed stepwise (20%) by charging at 2C. a) As illustrated by the dashed blue and the solid red line, the peak height between zero and 70 μs is invariant of the state-of-charge, while the peak height of the slower wave varies linearly. b) Delay time over signal height. The slow wave's delay time shows a linear dependence on state-of-charge, while the delay of the invariant, faster wave appears to be unchanged. (For interpretation of the references to colour in this figure legend, the reader is referred to the web version of this article.)

time-of-flight analogy. To illustrate this dependency, it is instructive to tilt the signal graphs already shown in Fig. 3 a). Fig. 3 b) shows the graphs with interchanged abscissa and ordinate, where the first wave is shown below, while the second wave is shown on top. The time-of-flight (delay time) of the fast wave once again appears unchanged, while the delay of the slow wave varies with the state-of-charge (red line).

To quantify peak height and position as a function of the state-of-charge, the delays and peak heights were estimated by peak picking of the smoothed and rectified signals shown in Fig. 3 a). For peak finding a local maximum method with a 12 μs window was used. Found peaks were filtered by height, thresholding at 20% of the data's maximum value. The obtained response delay of the fast wave is invariant to the state-of-charge while the delay of the slow wave is proportional to the state-of-charge.

3.1.4. Overview of changing signal properties

In Fig. 4 the results from quantifying peak height and time-of-flight are compared. The obtained answer signals contain a linear measure of the state-of-charge and a reference value. The first part of the responses shown in Fig. 4a) and b) can thus be used as an internal standard allowing to account for changes in the generated signal that are not related to the state-of-charge. This could be caused by a varying adhesion of the transducers or unstable voltage levels in the circuitry. The second part of the responses shown in Fig. 4c) and d) contains a measure for the state-of-charge.

In Fig. 5 the signal height of the slow pressure wave obtained by stepwise charging at 2 C is compared to those obtained from discharging at 4 C after a 30 min rest period at 100% SoC. A hysteresis is visible for partly charged states while the extrema of SoC, namely 0% and 100%, show a good agreement. Linear fitting the measurement points, acquired during stepwise charging, yields a coefficient of determination of 0.995. In the case of stepwise charging we calculated an average SoC estimation error of 3.5% SoC from a linear calibration curve. For discharging at a rate of 4 C, an error of 11.0% SoC was obtained. Clearly, a linear fit is not appropriate for the discharge characteristic. A more sophisticated calibration function that may significantly improve this value is currently under investigation. Observing a hysteresis is common for both mechanical [13,45] and electrical [46–49] properties of lithium-ion cells. Therefore, knowledge about the impact of hysteresis on the discovered phenomenon is desired. In more detail, the dependence of hysteresis upon C-rates and cycling history are of interest and will be targeted in future research.

3.2. Acoustic effects of the state-of-charge − comparison to theory

3.2.1. Effects on different scales

Biot's theory is especially successful in predicting the observable parameters of transmitted waves. Based on the mechanical properties of the porous network and the liquid, the theory discussed in Section 1.2 is used to predict the respective velocities of the three waves in fluid-filled porous media [18,19].

As a first step, velocities predicted for the porous graphite electrode are compared to the qualitative trend in experimental times-
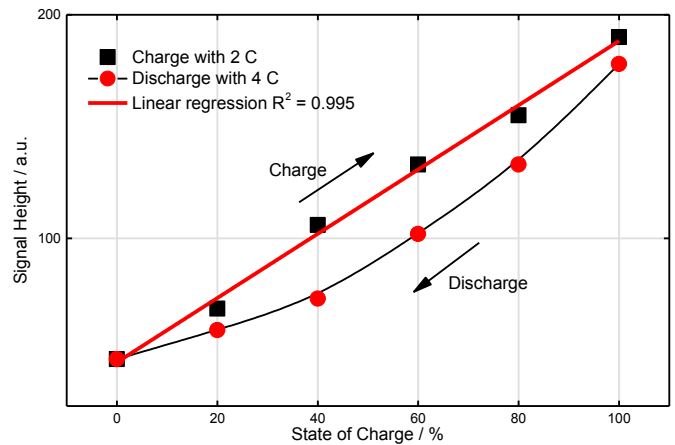

Fig. 5. Signal height for the slow compressional wave plotted as a function of the SoC: The signals obtained from stepwise quick charging at 2 C (black) show a linear dependence on the SoC while the signals obtained from stepwise discharging at 4 C (red) after a 30 min rest period at 100% SoC show a hysteresis. (For interpretation of the references to colour in this figure legend, the reader is referred to the web version of this article.)

of-flight measurements. Then, the wavelengths are compared to the characteristic length scales found in lithium-ion batteries. Based on these considerations, a hypothesis for the underlying attenuation mechanisms is developed.

To establish the phase velocities of the waves, it is necessary to establish their respective trajectories. Body waves are the easiest case, especially when the signal is focused along the normal axis of the transmitter. As the transducer planes are sufficiently large, placed parallel and centered, the trajectory of the pulses can be approximated by the distance of the transducers. Surface waves and reflected signals disturb the received signal, as they may travel along different paths causing delayed arrivals. For the following treatment it will be assumed that both slow and fast wave packets are body waves travelling along the normal axis, an assumption that will be corroborated in Section 3.2.3.

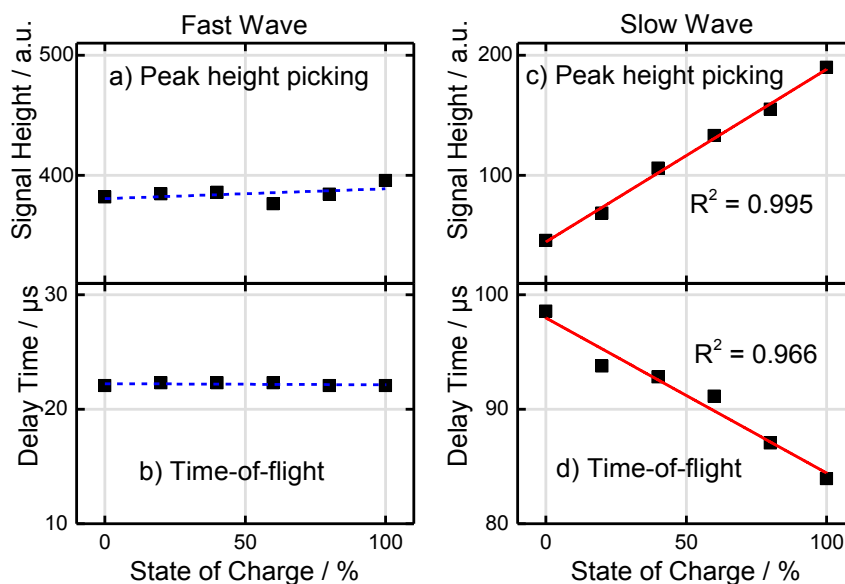**Fig. 4.** Peak heights and positions determined by local maximum method from smoothed and rectified data presented in Fig. 3 a): Peaks, assigned to slow and fast pressure wave, are compared in terms of signal height and peak position (delay). a) and b) show the invariance of peak height and time-of-flight (delay) of the fast wave, while c) and d) show the linear dependence on the state-of-charge of the slow wave.

3.2.2. Velocity change predicted by Biot's theory

It is well-known in literature that graphite electrodes change their mechanical properties during charging, leading to a nearly linear variation of cell parameters [50] and elastic moduli [51]. The phase velocities of the different waves are predicted using Biot's low frequency approximation discussed in detail in Section 1.2. All values for material parameters of a graphite electrode are listed in Appendix A, Table A 1. Most values were obtained from the litera-ture, while the shear modulus N_n as well as the bulk modulus k_b of the drained matrix were estimated from our data. The values for the fast and shear wave's velocities gave $V_I = 3220$ m s^{-1} and $V_s = 460$ m s^{-1}, respectively.

In a first attempt we try to understand the propagation of ul-trasonic waves through the complex structure of real lithium-ion cells. From the formulas provided in Section 1.2 and the parame-ters in Appendix A we calculated the velocities V_I and V_{II} in a graphite electrode as a function of porosity. In good agreement with the observed values the fast compressional wave's velocity V_I is found to be nearly constant with respect to porosity: a change from 40% to 15% porosity leads only to a slight decrease from 3220 m s^{-1} to 3098 m s^{-1} for V_I. Once again in good accordance with experi-mental findings, the velocity V_{II} of the slow wave is found to vary significantly. The estimated slow wave's velocity in the graphite electrode as well as expected delays calculated from the velocity and thickness of the cell, 7 mm, as well as the approximated dead time, 4.8 μs, and half peak broadness, 19 μs, are represented in Fig. 6. For this rough estimation, ultrasonic properties of the cell are assumed to be uniform over the whole cell and equal to the graphite elec-trode's properties. While for the investigated cell the exact porosity change is unknown, the observed change in delay time from 99 μs to 84 μs (see Fig. 4 d) would imply a porosity change from 30% to 20%. This compares well to typical porosities of approximately 30% in unlithiated state and absolute variations in the range of 15–20% [51].

As discussed in Section 1.2, Biot's theory has been successful in estimating phase velocities. But the apparent attenuation of the waves generally deviates from the predicted values due to the heterogeneity of real media. Therefore, the attenuation effects will be correlated to the change in wavelength induced by the velocity variation explained in the following section.

3.2.3. Scattering effects on boundaries

In 1991, Carcione summarized the general behavior of acoustic waves in stratified media [41]. Electrodes in lithium-ion batteries
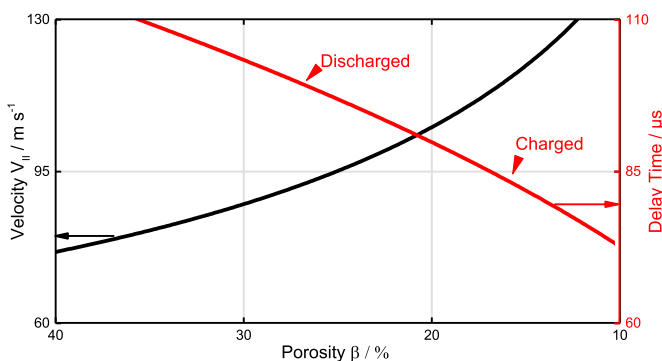
generally exhibit porosities in the order of few micrometers and layer thicknesses in the order of magnitude of a tenth of a millimeter [52]. The wavelength λ can be calculated from $\lambda = c/f$ with velocity c and frequency f. At 200 kHz, the wavelengths of the observed modes can be estimated to be greater than 20 mm for the fast wave and greater than 2 mm for the shear wave. As shown in the inlay of Fig. 7, the wavelength of the second pressure wave varies between 0.59 mm and 0.73 mm upon cycling through the state-of-charge.

According to the calculations provided by Carcione [41] the layered electrodes of the battery should appear as a smooth effective material to the fast compressional wave and the shear wave. However, as the wavelengths of slow pressure waves at the utilized frequencies are close to the layer thickness in lithium-ion batteries, we can expect that a change of wavelength, either by frequency or velocity, leads to changes in their behavior.

In this section, we will show that a variation of the ratio of wavelength over layer thickness does indeed yield comparable results, regardless whether it is caused by a variation in frequency or phase velocity.

The comparison of changes in the signal induced by frequency variations and cycling through the SoC in Fig. 7 explains the observed behavior. When the frequency is increased the signal is constant up to about 150 kHz. But as soon as the wavelength ap-proaches the order of magnitude of the layers, its attenuation suddenly increases dramatically. As discussed in the theoretical Section 1.2, this behavior is well-known and has been explained by scattering at the boundaries [41]. As shown in Section 3.2.2, charging and discharging the battery results in approximately linear velocity changes and, thus, also the signal height of the slow pressure wave does vary linearly. By varying the frequency, the range of the ratio of the wavelength over the layer thickness can be scaled. So, by optimizing the frequency, it is possible to place the ratio in a monotonously increasing range. Then, an increase in ve-locity goes along with an increase in transmitted amplitude.

While the dispersive behavior depends on the complex prop-erties of the porous materials and the interfaces, dispersion can be observed when the wavelength is sufficiently small compared to the effective periodic length of the heterogeneity [22,41].

The inlay in Fig. 7 shows that the change of velocity induced by cycling the cell leads to comparable effects as a change in frequency. This finding supports the theory that lithium intercalation changes
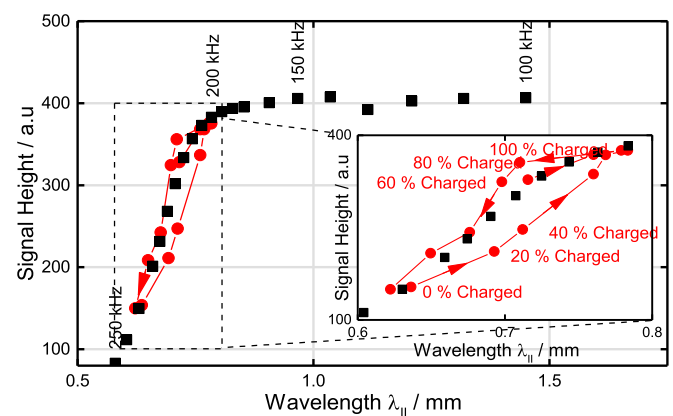
Fig. 6. Phase velocity V_{II} of Biot's second wave in graphite electrodes predicted as a function of porosity by Biot's theory according to material data given in Appendix A, Table A 1: From the velocity V_{II} and the cell thickness, 7 mm, the expected delay is approximated by taking a dead time of approximately 4.8 μs and a peak front broadness of approximately 19 μs. For this rough estimation, ultrasonic properties of the cell are assumed to be uniform for the whole cell and equal to the graphite elec-trode's properties. The observed trend compares well to experimental data obtained in Section 3.1.

Fig. 7. Height of the second wave's peak plotted versus wavelength λ_{II} of second compressional wave. Signal heights are compared upon variation of excitation fre-quency on a cell as received from the manufacturer (black squares) and a subsequent full charge cycle (red dots). The wavelength was varied by changing frequency and velocity. The inlay visualizes a similar effect of varying wavelength by cycling and frequency change. Once more the hysteresis induced by cycling is visible. (For inter-pretation of the references to colour in this figure legend, the reader is referred to the web version of this article.)

material parameters which in turn lead to velocity and wavelength variations that can finally result in dispersive effects. Therefore, this result implies that the method should be transferable to other cells containing non-zero-strain materials. <mark>Furthermore, this understanding helps finding the optimum frequency, as most useful signal variations can be obtained by choosing an excitation frequency yielding a wavelength in the transition to the scattering regime.</mark> This frequency, in which the ratio of wavelength over layer thickness is placed in a monotonously increasing range, can easily be found by a frequency variation experiment on a cell with known state-of-charge.

4. Conclusions

In this work, a new, direct method for state-of-charge (SoC) estimations is present: our approach is based on the observed linear correlation between ultrasonic pulse transmission and the actual state-of-charge. This new technology allows for a direct measurement of the state-of-charge for batteries with various positive active materials. Since the observed changes in ultrasonic pulse transmission can be correlated to the lithiation of graphite, the SoC can be determined without a reference electrode, i.e. "*model free*". As the lithiation of graphite is probed directly, the most critical system property is made accessible in commercial batteries under real use conditions. Furthermore, the method does not rely on electric measurements on the cell and offers due to rapid measurement sequential screening of batteries within battery packs. Therefore, single measurement logic, using multiplexing, could be a cost saving alternative to conventional cell level control.

Already at this early stage of development, the observed correlations allow for a good estimation of state-of-charge during charging with an average SoC estimation error of 3.5% SoC. The present hysteresis in the signal height of the slow wave, which is unneglectable especially during discharging at higher currents, will be subject to further investigation. Since ultrasonic pulses probe physical properties of LIBs, environmental and cycling parameters may influence the resulting transmission signal.

The observed signal dependency on SoC can be explained by the application of Biot's theory for propagation of waves in fluid-saturated porous media, combined with scattering effects on boundaries within the stratified medium "battery", in which lithiation leads to changes of physical properties such as porosity. To probe these changes, <u>the sensors were placed in the center of the cell's faces to avoid edge effects.</u> Still, it should be investigated to which extend edge-effects lead to errors, as scanning the surface could give access to SOC maps of cells for research purposes.

Future improvements on the method are currently investigated: comprising factors such as long-term behavior, battery aging, temperature, hysteresis and current rates as well as a proof of concept based on a low-cost microchip (to be published elsewhere). Furthermore, the application to batteries with very flat open circuit voltage (OCV) curves, such as those based on lithium-iron-phosphate and their SoC will be our next research target.

Acknowledgement

Glossary

List of abbreviations and acronyms
SoC   State-of-charge

ToF   Time-of-flight
LIB   Lithium-ion battery
BMS   Battery management system
RCN-pulses Raised cosine pulses with N oscillations
OCV   Open circuit voltage
EC   Ethylene carbonate
DMC   Dimethyl carbonate
LiPF6   Lithium hexafluorophosphate
LiPo   Lithium-ion battery with polymer based electrolyte

Appendices

A. Parameters and variables of Biot's theory

The velocity of the shear wave V_s is given by

$$V_s = \sqrt{\frac{N_n}{\rho_{11}\left(1-\frac{\rho_{12}^2}{\rho_{11}\,\rho_{22}}\right)}} \qquad (A.1)$$

where N_n is the shear modulus of the drained matrix and ρ_{11} and ρ_{22} denote mass coefficients and ρ_{12} denotes the coupling coefficient.

The mass of solid per unit volume ρ_1, mass of fluid per unit volume ρ_2, and the mean density ρ are given by the following equations, where β is the porosity, while ρ_f and ρ_s are the densities of fluid and solid, respectively [19]:

$$\rho_1 = (1-\beta)\rho_s \qquad (A.2)$$

$$\rho_2 = \beta\,\rho_f \qquad (A.3)$$

$$\rho = \rho_1 + \rho_2 \qquad (A.4)$$

The mass coefficients ρ_{11} and ρ_{22} [19] as well as the coupling coefficient ρ_{12} [22] are defined as a function of the tortuosity α,

$$\rho_{11} = \rho_1 - \rho_{12} \qquad (A.5)$$

$$\rho_{22} = \rho_2 - \rho_{12} \qquad (A.6)$$

$$\rho_{12} = -(\alpha-1)\,\beta\,\rho_f \qquad (A.7)$$

The effective porosity β_{eff} is given a function of the bulk moduli of the fluid k_f, solid k_s and porous drained matrix k_b [22]:

$$\beta_{eff} = \beta + \frac{k_f}{k_s}\left(1-\beta-\frac{k_b}{k_s}\right) \qquad (A.8)$$

The characteristic frequency.

$$f_c = \frac{b}{2\,\pi\,\rho\,(\gamma_{12}+\gamma_{22})} \qquad (A.9)$$

contains the coefficient b [19], which is a function of the dynamic viscosity μ of the fluid, the porosity β and Darcy's coefficient of permeability k given as [19]:

$$b = \mu\frac{\beta^2}{k} \qquad (A.10)$$

The parameters of dynamic properties are defined as follows [19]:

$$\gamma_{11} = \frac{\rho_{11}}{\rho} \qquad (A.\ 11)$$

$$R = \frac{\beta^2}{\beta_{eff}} k_f \qquad (A.\ 20)$$

$$\gamma_{22} = \frac{\rho_{22}}{\rho} \qquad (A.\ 12)$$

$$H = P + R + 2Q \qquad (A.\ 21)$$

Table A. 1
Parameters used for Biot theory. To investigate the behavior of the slow wave in a graphite electrode during charge, parameters from literature and own estimations were used.

Parameter	Abbr.	Value	Value obtained from
Shear modulus of drained matrix	N_n	0.392 GPa	Velocity of shear wave
Density of solid	ρ_s	2100 kg m^{-3}	Approximate value derived from Ref. [53]
Electrolyte Density 1.0 M LiPF6 in EC/EMC 1/1 (vol)	ρ_f	1270 kg m^{-3}	[54]
Tortuosity	α	2.5	Rough estimate due to anisotropy [55]
Darcy's coefficient of permeability	k	$4.0\ 10^{-14}$	[56]
Fluid viscosity	μ	42 mPa s	[56]
Porosity	β	0.1 to 0.4	[51]
Bulk modulus of fluid	k_f	1 GPa	[56]
Bulk modulus of solid	k_s	29.3 GPa	Based on [57]
Bulk modulus of porous drained matrix	k_b	17.4 GPa	Fast wave's velocity
Pore diameter	d	4 μm	Conservative approximation from scanning electron measurements
Parameters that depend on porosity β			
Mean density	ρ		Eq. (A. 2)
Mass of solid per unit volume	ρ_1		Eq. (A. 3)
Mass of fluid per unit volume	ρ_2		Eq. (A. 4)
Mass coefficients	ρ_{11}, ρ_{22}		Eq. (A. 5) and Eq. (A. 6)
Coupling coefficient	ρ_{12}		Eq. (A. 7)
Coefficient b	b		Eq. (A. 10)
Effective porosity	β_{eff}		Eq. (A. 8)
Characteristic frequency	f_c		Eq. (A. 9)
Parameters of dynamic properties	$\gamma_{11}, \gamma_{22}, \gamma_{12}$		Eq. (A. 11), Eq. (A. 12) and Eq. (A. 13)
Parameters defining elastic properties	$\sigma_{11}, \sigma_{22}, \sigma_{12}$		Eq. (A. 14), Eq. (A. 15) and Eq. (A. 16)
Reference velocity	V_c		$V_c = \sqrt{H/\rho}$

$$\gamma_{12} = \frac{\rho_{12}}{\rho} \qquad (A.\ 13)$$

While the parameters defining elastic properties, which are based on the Biot's parameters A, P, Q, R and H which correspond to the Lamé coefficients [19,22] are given by

$$\sigma_{11} = \frac{P}{H} \qquad (A.\ 14)$$

$$\sigma_{22} = \frac{R}{H} \qquad (A.\ 15)$$

$$\sigma_{12} = \frac{Q}{H} \qquad (A.\ 16)$$

Finally, the Biot's coefficients are defined by the following equations [22]:

$$A = k_b - 2\frac{N_n}{3} + \frac{k_f}{\beta_{eff}}\left(1 - \beta - \frac{k_b}{k_s}\right)^2 \qquad (A.\ 17)$$

$$P = A + 2 N_n \qquad (A.\ 18)$$

$$Q = \frac{\beta\ k_f}{\beta_{eff}}\left(1 - \beta - \frac{k_b}{k_s}\right) \qquad (A.\ 19)$$

B. Specifications

Table B. 1
Manufacturer's specifications of tested lithium-ion battery cells "Modellbau-Akku-pack (LiPo) 3.7 V 1200 mAh 20 C Conrad energy", Part-number: 683562-1200-20C.

Technology	LiPo
Nominal voltage	3.7 V
Capacity	1200 mAh
Max. discharge current (pulse)	48 A
Max. discharge current (continuous)	24 A
Max. charging current	2.4 A
Dimensions (height, wide, length)	7 mm, 36 mm, 67 mm

Table B. 2
Manufacturer's specifications of utilized piezo transducer. Specifications of the piezo element "Piezokeramisches Element EPZ-Serie - 6400 Hz", "EPZ-20MS64W", Part-number: 190031.

Materials	Ceramic on brass
Impedance	350 Ω
Resonance frequency	6400 Hz
Dimensions (outer diameter, electrode diameter, thickness)	20 mm, 15 mm, 0.19 mm
Capacitance	13 nF

Table B. 3
A Selection of manufacturer's specifications of used solvent-free, epoxy resin based two component adhesive "UHU plus endfest 300".

Chemical basis	Epoxy resin
Adhesive technique	Wet adhesion
Temperature range of use	−40 to +100 °C
Basis of binder	Epoxy resin
Basis of hardener	Aliphatic amines
Mixing ratio	1:1 (other ratios possible)

References

[1] S.F. Schuster, T. Bach, E. Fleder, J. Müller, M. Brand, G. Sextl, A. Jossen, J. Energy Storage 1 (2015) 44–53.
[2] V.A. Sethuraman, L.J. Hardwick, V. Srinivasan, R. Kostecki, J. Power Sources 195 (2010) 3655–3660.
[3] M. Ecker, N. Nieto, S. Käbitz, J. Schmalstieg, H. Blanke, A. Warnecke, D.U. Sauer, J. Power Sources 248 (2014) 839–851.
[4] M. Berecibar, I. Gandiaga, I. Villarreal, N. Omar, J. van Mierlo, P. Van den Bossche, Renew. Sustain. Energy Rev. 56 (2016) 572–587.
[5] L. Lu, X. Han, J. Li, J. Hua, M. Ouyang, J. Power Sources 226 (2013) 272–288.
[6] T. Huria, G. Ludovici, G. Lutzemberger, J. Power Sources 249 (2014) 92–102.
[7] W.-Y. Chang, ISRN Appl. Math. 2013 (2013) 1–7.
[8] A. Senyshyn, O. Dolotko, M.J. Muhlbauer, K. Nikolowski, H. Fuess, H. Ehrenberg, J. Electrochem. Soc. 160 (2013) 3198–3205.
[9] T. Ohzuku, N. Matoba, K. Sawai, J. Power Sources 97–98 (2001) 73–77.
[10] D. Billaud, F.X. Henry, M. Lelaurain, P. Willmann, J. Phys. Chem. Solids 57 (1996) 775–781.
[11] Y. Qi, L.G. Hector, C. James, K.J. Kim, J. Electrochem. Soc. 161 (2014) 3010–3018.
[12] L.W. Sommer, P. Kiesel, A. Ganguli, A. Lochbaum, B. Saha, J. Schwartz, C.-J. Bae, M. Alamgir, A. Raghavan, J. Power Sources 296 (2015) 46–52.
[13] B. Bitzer, A. Gruhle, J. Power Sources 262 (2014) 297–302.
[14] J. Cannarella, C.B. Arnold, J. Power Sources 245 (2014) 745–751.
[15] J. Cannarella, C.B. Arnold, J. Power Sources 269 (2014) 7–14.
[16] A.G. Hsieh, S. Bhadra, B.J. Hertzberg, P.J. Gjeltema, A. Goy, J.W. Fleischer, D.A. Steingart, Energy Environ. Sci. 8 (2015) 1569–1577.
[17] K.J. Langenberg, R. Marklein, K. Mayer, Ultrasonic Nondestructive Testing of Materials: Theoretical Foundations, CRC Press, 2012.
[18] M.A. Biot, J. Acoust. Soc. Am. 28 (1956) 179–191.
[19] M.A. Biot, J. Acoust. Soc. Am. 28 (1956) 168–178.
[20] K.N. van Dalen (Ed.), Multi-component Acoustic Characterization of Porous Media, Springer Berlin Heidelberg, Berlin, Heidelberg, 2013.
[21] M. Weller, T. Overton, J. Rourke, F.A. Armstrong, Inorganic Chemistry, sixth ed.
[22] J. Jocker, D. Smeulders, Ultrasonics 49 (2009) 319–330.
[23] M. Pakula, F. Padilla, P. Laugier, M. Kaczmarek, J. Acoust. Soc. Am. 123 (2008) 2415–2423.
[24] C.M. Langton, C.F. Njeh, IEEE Trans. Ultrasonics, Ferroelectr. Freq. Control 55 (2008) 1546–1554.
[25] T.J. Plona, Appl. Phys. Lett. 36 (1980) 259.
[26] Z.A. Fellah, N. Sebaa, M. Fellah, F.G. Mitri, E. Ogam, W. Lauriks, C. Depollier, IEEE Trans. Ultrasonics, Ferroelectr. Freq. Control 55 (2008) 1508–1515.
[27] T.E. Gómez Alvarez-Arenas, E. Riera-Franco de Sarabia, F.R. Montero de Espinosa-Feijo, Ultrasonics 32 (1994) 131–140.
[28] T.E. Gómez-Alvarez Arenas, E. Riera Franco De Sarabia, J. Phys. IV Fr. 04 (1994). C5-187-C5-190.
[29] K.I. Lee, S.W. Yoon, J. Biomech. 39 (2006) 364–368.
[30] L.A. Molotkov, A.V. Bakulin, J. Math. Sci. 96 (1999) 3371–3385.
[31] J.O. Parra, J. Acoust. Soc. Am. 95 (1994) 91–98.
[32] S.R. Pride, E. Tromeur, J.G. Berryman, Geophysics 67 (2002) 271–281.
[33] J.G. Berryman, PAGEOPH 128 (1988) 423–432.
[34] B. Gurevich, D. Makarynska, de Paula, Osni Bastos, M. Pervukhina, Geophysics 75 (2010) N109–N120.
[35] J. Dvorkin, R. Nolen-Hoeksema, A. Nur, Geophysics 59 (1994) 428–438.
[36] W.F. Murphy, K.W. Winkler, R.L. Kleinberg, Geophysics 51 (1986) 757–766.
[37] A.N. Norris, J. Acoust. Soc. Am. 94 (1993) 359–370.
[38] S. Gelinsky, S.A. Shapiro, T. Müller, B. Gurevich, Int. J. Solid Struct. 35 (1998) 4739–4751.
[39] T.M. Müller, B. Gurevich, M. Lebedev, Geophysics 75 (2010) 75A147.
[40] J.B. Walsh, J. Geophys. Res. 74 (1969) 4333–4337.
[41] J.M. Carcione, D. Kosloff, A. Behle, Geophysics 56 (1991) 245–254.
[42] J.E. White, J. Acoust. Soc. Am. 57 (1975) 654–659.
[43] H. Ren, G. Goloshubin, F.J. Hilterman, Geophysics 74 (2009) N49–N54.
[44] B.B.S.A. Vogelaar, Fluid Effect on Wave Propagation in Heterogeneous Porous Media, Dissertation, Delft, 2009.
[45] V. Sethuraman, N. van Winkle, D.P. Abraham, A. Bower, P. Guduru, J. Power Sources 206 (2012) 334–342.
[46] N. Nitta, F. Wu, J.T. Lee, G. Yushin, Mater. Today 18 (2015) 252–264.
[47] W. Dreyer, J. Jamnik, C. Guhlke, R. Huth, J. Moskon, M. Gaberscek, Nat. Mater. 9 (2010) 448–453.
[48] C. Zhang, J. Jiang, W. Zhang, S.M. Sharkh, Energies 5 (2012) 1098–1115.
[49] M.A. Roscher, O. Bohlen, J. Vetter, Int. J. Electrochem. 2011 (2011) 1–6.
[50] S.J. Harris, P. Lu, J. Phys. Chem. C 117 (2013) 6481–6492.
[51] Y. Qi, S.J. Harris, J. Electrochem. Soc. 157 (2010) 741–747.
[52] M. Singh, J. Kaiser, H. Hahn, J. Electrochem. Soc. 162 (2015) A1196–A1201.
[53] H.C. Howard, G.A. Hulett, J. Phys. Chem. 28 (1923) 1082–1095.
[54] Sigma-Aldrich, Product Specification: Lithium Hexafluorophosphate Solution in Ethylene Carbonate and Ethyl Methyl Carbonate, 1.0 M LiPF6 in EC/EMC=50/50 (V/v), Battery Grade Specification Sheet.
[55] M. Ebner, D.-W. Chung, R.E. García, V. Wood, Adv. Energy Mater. 4 (2014) (n/a).
[56] G.Y. Gor, J. Cannarella, J.H. Prevost, C.B. Arnold, J. Electrochem. Soc. 161 (2014) 3065–3071.
[57] Y. Qi, H. Guo, L.G. Hector, A. Timmons, J. Electrochem. Soc. 157 (2010) 558–566.